



# The effect of counter electrodes on the photodegrading performances of azoic dye using TiO<sub>2</sub> nanotubes arrays

Abdulaziz M. J. Alshareef<sup>1</sup>, Md. Faruk Hossain<sup>2,\*</sup> , Mohammad Mostafizur Rahman Biswas<sup>2</sup>, and Ibrahim Mustafa Mehedi<sup>1,3</sup>

<sup>1</sup>Department of Electrical and Computer Engineering (ECE), King Abdulaziz University, Jeddah 21589, Saudi Arabia

<sup>2</sup>Department of Electrical and Electronic Engineering, Rajshahi University of Engineering & Technology, Rajshahi, Bangladesh

<sup>3</sup>Center of Excellence in Intelligent Engineering Systems (CEIES), King Abdulaziz University, Jeddah 21589, Saudi Arabia

**Received:** 11 September 2020

**Accepted:** 20 July 2021

**Published online:**

13 August 2021

© The Author(s), under exclusive licence to Springer Science+Business Media, LLC, part of Springer Nature 2021

## ABSTRACT

The novelty of this work is to fabricate the double-walled (DW) TiO<sub>2</sub> nanotube arrays (TNAs) by an anode oxidation method with NH<sub>4</sub>F-based electrolyte and Zinc counter electrode (CE, c-Zn) and to investigate the photodegradation performance of these TNAs. The structural, optical, and photodegradation performance of TNAs with c-Zn material have been compared to the properties of TNAs with the other two CEs like c-Pt (Platinum) and c-Ti (Titanium). The counter electrode has a tremendous influence on the structural properties and geometrical features of TNAs. The TNAs fabricated with c-Zn have the red-shifted absorption edge with two bandgaps such as 3.15 and 1.78 eV. Interestingly, the TNAs with c-Zn are found as the DW TNAs with outer diameter of  $130 \pm 3$  nm, thinner outer wall thickness of  $12 \pm 2$  nm, and thicker inner wall thickness of  $30 \pm 2$  nm. The photodegradation performance varies with different counter electrodes during the deposition of TNAs by the anode oxidation method. The TNAs sample prepared with c-Zn has shown the highest roughness value of 305.0 nm, photodegradation efficiency of 97.0%, and the rate constant value of  $0.00985 \text{ min}^{-1}$  than the other TNAs with c-Pt, c-Ti, and other researcher's data. Moreover, the optical, structural, and surface morphological properties of TNAs have correlated with the photodegradation performance of TNAs prepared with various counter electrodes during deposition.

Address correspondence to E-mail: engr.mfhossain@eee.ruet.ac.bd; faruk94\_ruet@yahoo.com

## 1 Introduction

The wastewater is contaminated with different inorganic and organic pollutants or dyes discharged from textiles, agricultural, factories, and printing industries [1–4]. Organic dyes or azoic dyes are hazardous and created environmental problems because of the toxicity, mutagenicity, and carcinogenicity [5] that increase the chemical oxygen demand and alter the pH value of water in ecosystems [6]. In recent years, wastewater treatment is a crucial concern to ensure a healthy environment [1].

There are some convenient methods for removing pollutants or dyes from the wastewater, like sedimentation, filtration, chemical coagulation [6], biosorption [7], biological treatments (sequential bed reactors, bacterial culture, fungal species, activated sludge technique, and anaerobic/anoxic processes) [8, 9], adsorption [10], ozonation [11], wet oxidation [12], microwave irradiation [13], and membrane process [14]. However, the significant shortcoming of these methods is that the photocatalyst cannot eliminate all the pollutants [15] of wastewater. Moreover, these methods have high installation and operating costs. Recently, photocatalytic degradation has a great attraction due to degradation of the organic pollutants in wastewater under ambient pressure and temperature conditions [16, 17]. Additionally, this process can transform organic pollutants such as azoic dye into harmless carbon dioxide, water, and some mineral acid [6].

The photodegradation technique is involved with  $\text{TiO}_2$  under ultraviolet (UV)-visible illumination that primarily attributes to the photogeneration of electrons ( $e^-$ ) and holes ( $h_{vb}^+$ ) as well as the subsequent generation of reactive oxygen species (ROS). The ROS such as singlet oxygen ( ${}^1\text{O}_2$ ), superoxide anion ( $\text{O}_2^-$ ), hydroxyl radicals ( $\text{HO}\cdot$ ), per hydroxyl radical ( $\text{HO}_2\cdot$ ), and hydrogen peroxide ( $\text{H}_2\text{O}_2$ ) are capable of selectively or nonselectively oxidizing and mineralizing a broad range of organic pollutants [18, 19].

In the past few decades, high efficiency and stable photocatalytic materials extensively investigate to degrade organic pollution, and their potential applications to environmental remediation have been developed [20–22]. The  $\text{TiO}_2$  is the most utilized and promising photocatalyst [23] used to degrade the various kinds of toxic organic pollutants [24] because of its excellent properties such as wide bandgap, low cost, high oxidizing property, high thermal stability,

non-toxic with high chemical durability, high photochemical stability, super hydrophilicity, as well as favorable optoelectronic properties [25–29]. Over the past years, large-scale self-assembly of micro- and nanostructured building components has attracted significant interest in the materials of  $\text{TiO}_2$  [30].

Therefore, a highly efficient  $\text{TiO}_2$  photocatalyst requires a large surface area for degrading a high amount of dye and needs tailored microstructures for the fast electron transporting and light-harvesting properties [31]. The  $\text{TiO}_2$  nanotube arrays (TNAs) are the promising photocatalysts due to their high pore volume due to their open mesoporous nature, defect free, and highly vertical alignment [32] of nanostructures. TNA has also improved electron collection efficiency as a significance of fast electron transport [24]. The TNAs have been prepared by various fabrication methods, including sol-gel [33], sonochemical deposition, electrodeposition, template synthesis [34], hydrothermal synthesis [34], microwave irradiation [35], atomic layer deposition [36], and anodic oxidation [37].

Among these techniques, the anode oxidation method is a relatively simple and inexpensive process for the deposition of TNAs [32]. Therefore, researchers are trying to determine the most effective option of the anode oxidation process to get the best high-aligned TNAs [23, 38]. The TNA has an excellent charge separation facility which may be caused by the absence of grain boundaries [16]. Moreover, the TNA has good mechanical and chemical stability because it directly produces Ti substrate and good corrosion resistance.

The TNAs are expected to be a promising photocatalyst to overcome the drawbacks mentioned above due to their special chemical and physical characteristics, high specific area, and high pore volume due to their open mesoporous nature [23, 39]. Some researchers have already observed the effect of the electrochemical sweep rate, oxidation time, anodization potential, electrolyte concentration, and other important factors on the TNAs during the anode oxidation process [40]. Recently, TNAs are fabricated with various anodization voltage and different temperatures in electrolytes [41]. Also, the effect of anodization voltage, electrolyte, and time has been considered to fabricate the TNAs [42]. Additionally, some researchers have also investigated the effect of different cathode materials, including Pt [43], Fe [43, 44], C [43–45], W [45], Al [44], Ni [45], Co [43, 45],

Cu [45], Ta [45], Pd [43, 45], Sn [45], and stainless steel [44] on the morphology of TNAs. To the best of my knowledge, cathode materials titanium (c-Ti) and zinc (c-Zn) have not been used as a counter electrode during the anode oxidation method. Moreover, the main novelty of this work is to fabricate double-walled (DW) TNAs using a c-Zn (zinc) counter electrode. The double-walled TNAs have a large surface area and materials content that facilitate the electron transfer, resulting in better photodegradation of azoic dye [46].

So in this work, TNAs have been fabricated on a pure Ti sheet (99.99%) using electrochemical anode oxidation method with three counter electrodes (CEs) including c-Pt, c-Ti, and c-Zn metal sheet. The effect of using these counter electrodes on the surface morphological, optical, and structural properties of TNAs has been discussed and correlated with the photodegradation properties of the azoic dye.

## 2 Experimental section

### 2.1 Fabrication of $\text{TiO}_2$ nanotube arrays (TNAs)

The electrochemical anode oxidation method was used to fabricate the  $\text{TiO}_2$  nanotube arrays (TNAs). The detailed experimental setup of electrochemical anodic oxidation with a water-based cooling system for  $\text{TiO}_2$  NT array growth was elaborately discussed in our previous article [23, 38]. At first, the titanium sheets ( $2 \times 2$  cm, 0.2 mm thick, 99.99% pure) were cleaned with acetone and distilled water in an ultrasonic bath for 5 min and then dripped in an acidic mixture of HF:HNO<sub>3</sub>:H<sub>2</sub>O in 1:4:5 in volume for 30 s. After that, it was cleaned successively by soap treatment, acetone, and distilled water as mentioned in our previous work [23]. The two-electrode electrochemical anode oxidation setup had used Ti sheet as an anode and different metal foils as the cathode materials. Three metal foils/sheets are used as cathode materials/counter electrodes, including c-Pt, c-Ti, and c-Zn. The applied potential is 50 V, and the inter-electrode distance was 2.0 cm. The electrolyte content was ethylene glycol (EG), mixed with 0.3 wt% of NH<sub>4</sub>F and 3 (three) vol% of water. During deposition, the electrolyte solution was stirred at a speed of 60 revolutions per minute. The current versus time behavior curves under constant potential

had recorded using a Keithley 2400 source-meter unit. The samples were washed with distilled water after deposition and dried by air for an hour. The fabricated TNAs were annealed in dry oxygen at 450 °C for a half-hour with a heating/cooling rate of 2 °C/min.

### 2.2 Characterization of TNA's

The structural properties of the TNAs were observed by X-ray diffraction (XRD) analysis with data collected from XRD-6000 (SHIMADZU) using Cu-K $\alpha$  ( $\lambda = 1.54060$  nm) line with 40 kV–20 mA. The data were measured from  $2\theta$  values of 10°–80° with a step, 0.02°. The optical property of the TNAs was examined by defusing reflectance-mode spectrophotometer (UV-Vis-NIR 3100, SHIMADZU) within the wavelength range 300–900 nm at room temperature. The surface morphological properties were studied using a field emission scanning electron microscope (FE-SEM, JEOL, FE-SEM 6700F), atomic force microscopy (AFM, Park system XE 70), and transmission electron microscopy (TEM, EM-002B, TOP-CON Co. Ltd.). The X-ray photoelectron spectroscopy (XPS) measurement of  $\text{TiO}_2$  photoelectrode was carried out by Thermo Fisher Scientific XPS (EXCALAB 250Xi) spectroscopy using MgK $\alpha$  radiation. The chemical composition in wt% and compositional morphology were also estimated by energy-dispersive spectroscopy (EDS, JED 2200) equipped with a FE-SEM microscope.

### 2.3 Photodegradation of azoic dye

The photocatalytic property of the TNAs was confirmed using the degradation of an azoic dye like methylene blue (MB) dye ( $\text{C}_{16}\text{H}_{18}\text{ClN}_3\text{S}$ ) in an aqueous solution [27]. TNAs photocatalyst was dipped in a 50 mL aqueous solution of 10 mg·L<sup>-1</sup> MB. Before starting the irradiation, the MB-catalyst solution was stirred in a dark condition for a half-hour. Photodegradation experiments were carried out by exposing to an artificial solar simulator (a SOLAX lamp, model: SET-140F, SERIC Ltd.) with danger ultraviolet-cut (< 280 nm) filter [47]. The photodegradation of MB was tracked with a spectrophotometer (UV-Vis Jasco V-550) at a 665 nm wavelength (maximum absorbance for MB). The absorbance spectrum (300–900 nm) of azoic dye (MB) degradation using TNAs samples after 2-h treatment

with a 20-min interval. It observed that the highest peak of textile dye has occurred at a wavelength of 665 nm (UV light), and the full vigilance range is 620 nm to 690 nm.

### 3 Results and discussions

Figure 1 shows the current transient ( $J-t$ ) behavior recorded during the anodization process of the Ti sheet. The behavior of the  $J-t$  curve varies with the different counter electrodes such as c-Pt, c-Ti, and c-Zn. The recording of current density ( $\text{mA}/\text{cm}^2$ ) starts with the voltage ramp (0–50 V). Initially, the current-density profile during the deposition method for all counter electrodes increases sharply in a short time, which may be due to increased voltage (5 ~ 50 V). Among them, the current density with c-Zn cathode has the maximum overshoot peak.

After that,  $J$  is decreasing exponentially due to field-assisted oxidation of Ti formed into a thin, compact  $\text{TiO}_2$  film, where  $\text{TiO}_2$  film is more stable than Ti surface during anodization [48, 49]. In this stage, the electrochemical formation rate of  $\text{TiO}_2$  film is more than the chemical dissolution of Ti and  $\text{TiO}_2$ , which is making a thicker  $\text{TiO}_2$  layer [45]. The  $J$  for c-Ti cathode material is decreased very fast, which means that  $\text{TiO}_2$  becomes thicker than the current of other cathode materials, whereas the current for c-Zn cathode has decreased at a slow rate which means that  $\text{TiO}_2$  films are having less thickness.

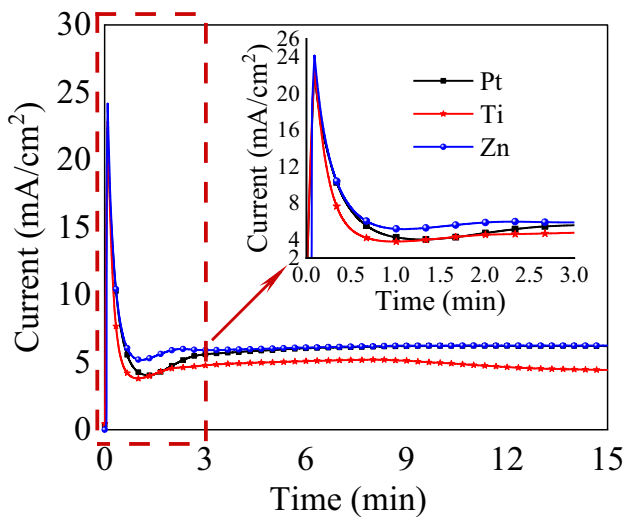


**Fig. 1** Current versus time of anode oxidation method with different counter electrodes

The current,  $J$  is started to increase up to a certain point, then the  $J$  is followed by a mild increase of current, which means that the randomly drilling of pits and pores in the surface of  $\text{TiO}_2$  film by fluoride ( $\text{F}^-$ ) ions. Finally, the current profile has found a steady-state value (significantly > zero), where the TNAs grow uniformly under these stable conditions [49].

The anodization current for the counter electrode c-Ti (red line) is showing that the etching starts after 63 s and the current profile decreased after 480 s, which indicates the ununiformed deposition rate due to high pitting of fluoride ( $\text{F}^-$ ) ion. Moreover, the blue and black colors (c-Zn and c-Pt) showed the steady-state flow of current (after 160 s) and reasonable etching rate, which indicated the uniform deposition and growth of TNAs. These two anodization currents are showing the fastest reaching of steady-state level with the constant current profile. On the other hand, the counter electrode c-Pt and c-Zn are better for the constant growth of TNAs [48]. The overpotential of the CEs is a key factor that affects the dissolution kinetics of the Ti anode, in turn controlling the activity of the electrolyte and morphology of the formed architectures [43].

Figure 2 shows the structural properties of TNAs prepared with various cathode materials. The crystallinity of TNAs varies with the different counter electrodes. All the diffraction peaks are indexing for the anatase phase (JCPDS card: 21-1272) and for the rutile phase (JCPDS card: 21-1276). It is clearly

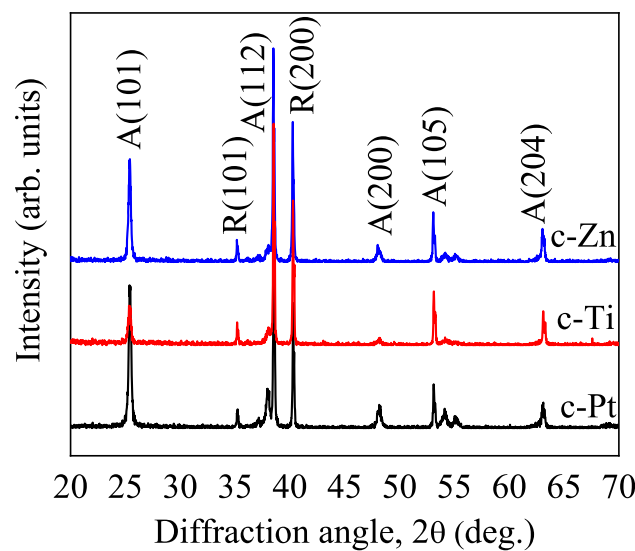


**Fig. 2** XRD patterns of TNAs prepared with different CEs

observed that the TNAs is polycrystalline in nature with almost anatase phase including two rutile phases. The pure anatase phase of A(101), A(112), A(200), A(105), and A(204) are observed at  $2\theta$  values of  $25.28^\circ$ ,  $38.57^\circ$ ,  $48.04^\circ$ ,  $53.89^\circ$ , and  $62.68^\circ$ , respectively. Moreover, two rutile peaks of R(101) and R(200) are found at the phase angle of  $36.08^\circ$  and  $41.18^\circ$ , respectively. The TNAs prepared with c-Ti have comparatively the lowest crystallinity than the others. The crystallite size has been calculated by Debye Scherrer's equation [50, 51].

$$d = \frac{0.94\lambda}{\beta \cos\theta} \quad (1)$$

where,  $\lambda$  is the wavelength of the X-ray ( $1.54 \text{ \AA}$ ),  $\beta$  is the full width at the half maximum (FWHM) of the peak, and  $\theta$  is the diffraction peak angle.

The crystalline size of TNAs has been calculated by Eq. (1) for both reflection peaks of A(101) and R(101). The size of crystallite data is listed in Table 1. For the A(101) peak, the crystallite size of TNAs prepared by anodization method with c-Pt, c-Zn, and c-Ti materials is 19, 18, and 14 nm, respectively; and for the R(101) peak, the crystalline size was 8 nm, 8 nm, and 3 nm for the reflection [101], respectively. The best crystalline size is observed for the counter electrode of c-Pt, c-Zn, and c-Ti. The FWHM value is small, which indicates that the crystallinity of TNAs improves [52].

The XPS analysis has investigated the chemical states of  $\text{Ti}_4^+$  in  $\text{TiO}_2$  films. Figure 3a and b shows the Ti 2p and O 1s spectra of TNAs prepared with different CEs of c-Pt, c-Ti, and c-Zn. From Fig. 3a, the binding energies (BEs) of two spin-orbit components, the peaks of  $\text{Ti } 2p_{3/2}$  and  $\text{Ti } 2p_{1/2}$  for TNAs with CEs (c-Pt and c-Ti), are shown at around 458.69 and at around 464.49 eV, respectively, which means that the existence of  $\text{Ti}_4^+$  (458.7 eV) ions of the pure  $\text{TiO}_2$  films, which may cause high crystallinity in nature

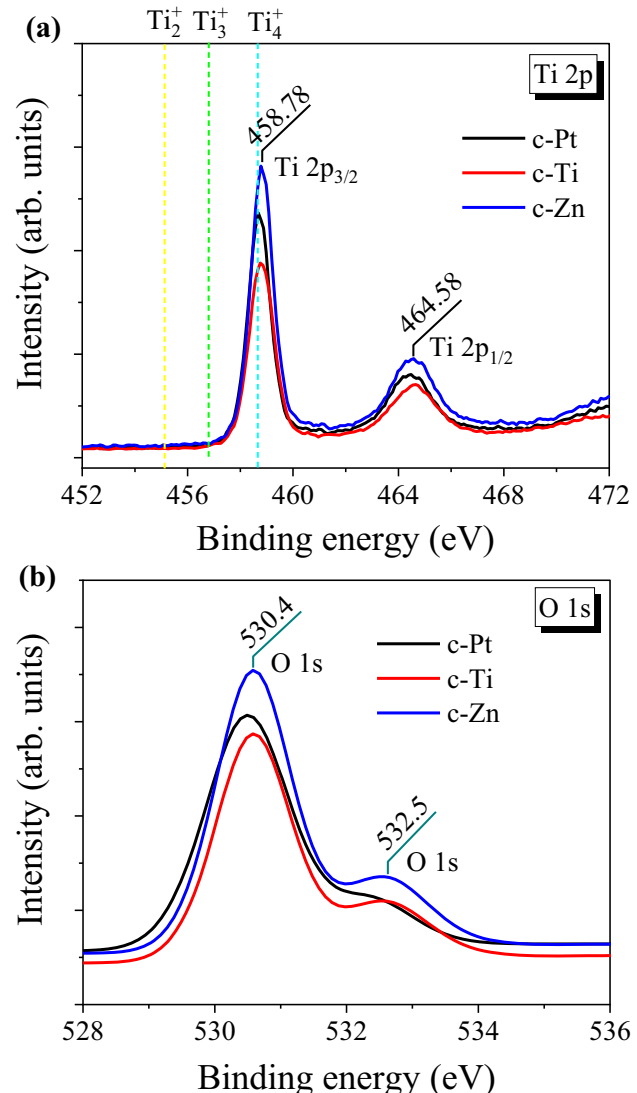


**Fig. 3** XPS curve of **a** Ti 2p and **b** O 1s spectra of TNAs prepared with different CEs

[53]. These peaks ( $\text{Ti } 2p_{3/2}$  and  $\text{Ti } 2p_{1/2}$ ) of TNAs prepared with c-Zn have been positively shifted to 458.79 eV and to 464.58 eV, respectively, which may be caused due to formation of high crystallinity [as

**Table 1** Structural and optical bandgap of TNAs prepared with different CEs

CEs	FWHM ( $\beta$ )	$d$ (nm) for A(101)	$d$ (nm) for R(101)	Inner (nm)	Outer (nm)	Porosity	Roughness factor, $\phi_{rf}$	$r_{ms}$ Roughness (nm)	$r_{ms}$ Roughness (nm) measured by AFM	Eg (eV)	
										1st	2nd
c-Pt	$7.72 \times 10^{-2}$	19.03	8.13	100	150	0.9798	0.00161	295.1	312	3.26	—
c-Ti	$10.52 \times 10^{-2}$	14.32	3.23	60	100	0.9773	0.00151	297.7	335	3.22	—
c-Zn	$8.06 \times 10^{-2}$	18.21	8.39	45	130	0.9794	0.00114	305.0	357	3.15	1.78

shown in Fig. 2] and n-doped TiO<sub>2</sub> films [54]. Figure 3b presents the O 1s spectrum of TNAs with all CEs, which is asymmetric O1s peak located at 530.5 ~ 530.58 eV, which corresponds to lattice oxygen of TiO<sub>2</sub>, and is consistent with previous studies of TiO<sub>2</sub> [53].

Figure 4a exhibits the EDS spectrum of the TNAs, prepared by anode oxidation with three different CEs. From the EDS spectrum, the peaks of Ti, O, and C are found. For TNAs with all CEs, the peak of Ti and O validated that the composition of these products has high purity [52]. Table II (inset of Fig. 4a) displays the chemical composition (weight in percentage, wt%) and the molar ratio of Ti:O for the TNAs prepared by the anode oxidation method with different CEs. These data have good agreement with XPS results (as shown in Fig. 3). Figure 4b shows the

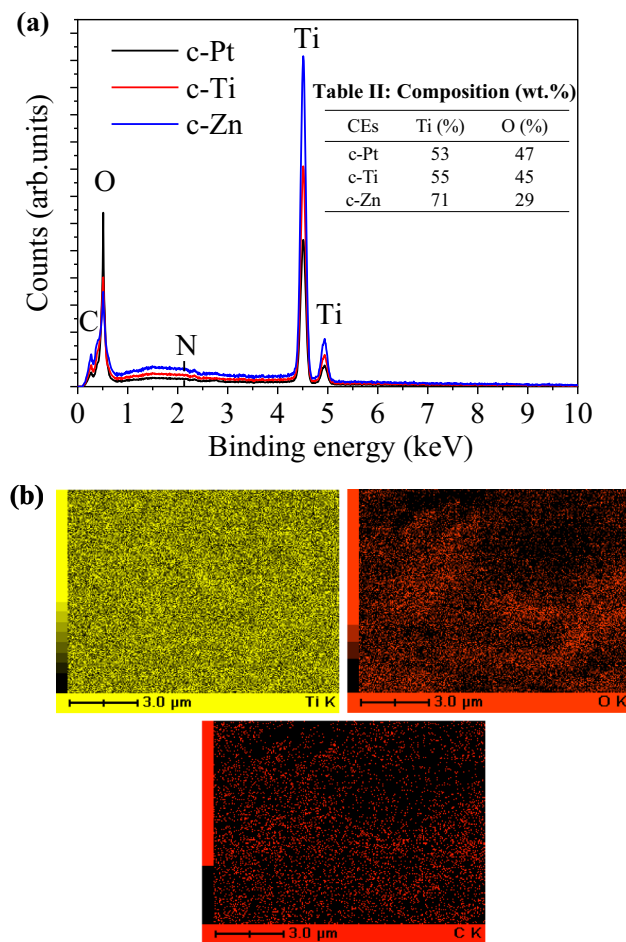


**Fig. 4** a EDS data of TNAs prepared with different CEs. b The mapping data of Ti, O, and C elements in the surface of TNAs with Zn CE

elemental composition with color mapping of Ti, O, and C.

Figure 5a displays the absorbance spectra of TNAs as a function of wavelength with the range of 300–900 nm. The CEs materials have a great influence on the absorbance of TNAs. All the spectra show low absorption with a sharp increase of absorbance, which identifies the high crystallinity of the films. The absorbance spectrum of TNAs with Ti has the absorption peak and the overall higher value than the other CEs (c-Pt and c-Zn) in the whole wavelength range. This TNA has a single absorption edge at the wavelength 380 nm, which corresponds to a 3.26 eV (as shown in Table II) bandgap. It observes that the absorbance of the TNAs sample prepared with c-Pt has the lowest absorption peak and has a higher absorbance value than the TNAs sample with c-Zn.

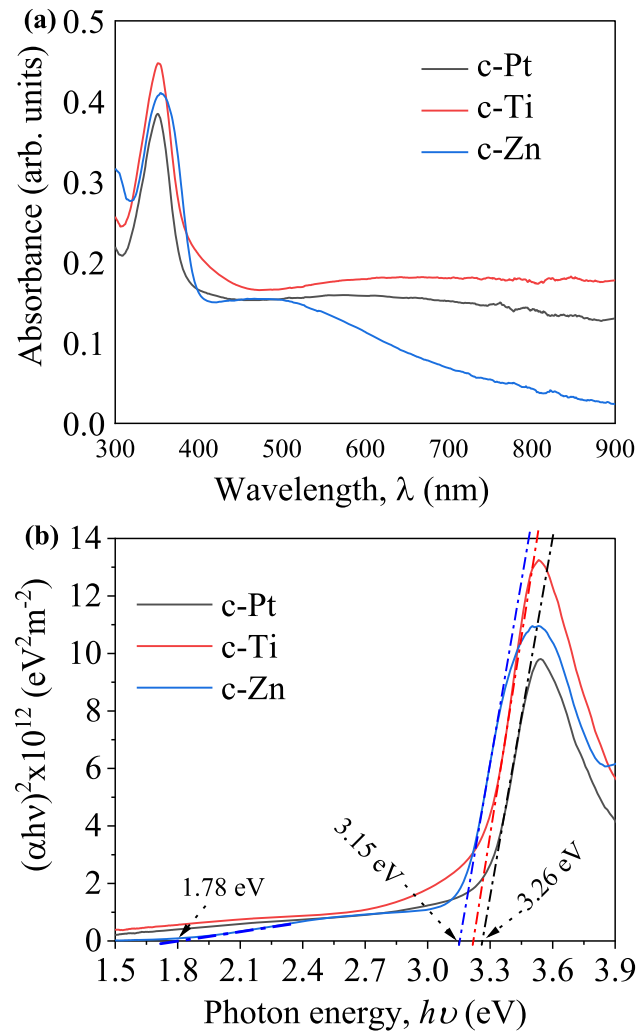


**Fig. 5** a Absorbance spectra and b  $(\alpha h\nu)^2$  versus  $h\nu$  of TNAs prepared with different counter electrodes

Moreover, these TNAs also have a single absorption edge at 385 nm, corresponding to a 3.22 eV bandgap (as given in Table II). It has cleared that the absorbance edges show a little red shift with different CEs of c-Pt, c-Ti, and c-Zn. The TNAs fabricated with c-Zn material not only showed the typically initial absorption edge at the near UV region but also showed an absorption peak in the visible region due to the nitrogen incorporation [55].

The relation between the absorption coefficients and the incident photon energy of the semiconductors is given by Eq. (1) [55]:

$$(\alpha h\nu) = A(h\nu - E_g)^n \quad (2)$$

where  $\alpha$  is the absorption coefficient,  $A$  is a constant,  $h\nu$  is the photon energy, and  $n$  is 0.5 and 2.0 for direct and indirect transition semiconductors, respectively. The  $TiO_2$  has the direct transition bandedge [55] so that  $n = 0.5$  is used in Eq. (2). The linear fit in  $(\alpha h\nu)^2$  versus  $h\nu$  is shown in Fig. 5b. The TNAs samples with c-Pt and c-Ti have the extrapolated direct optical main bandgap of 3.26 and 3.22, respectively. But TNAs with c-Zn have the two bandgaps, such as bandgaps of 3.15 eV and sub-bandgap of 1.78 eV, which indicate that the optical bandgap is significantly narrow due to double-walled TNAs and maybe incorporation of the nitrogen [55].

The PL spectra of the TNAs prepared with different CEs are shown in Fig. 6. Generally, the PL spectrum has two parts: the ultraviolet (UV) peak and the

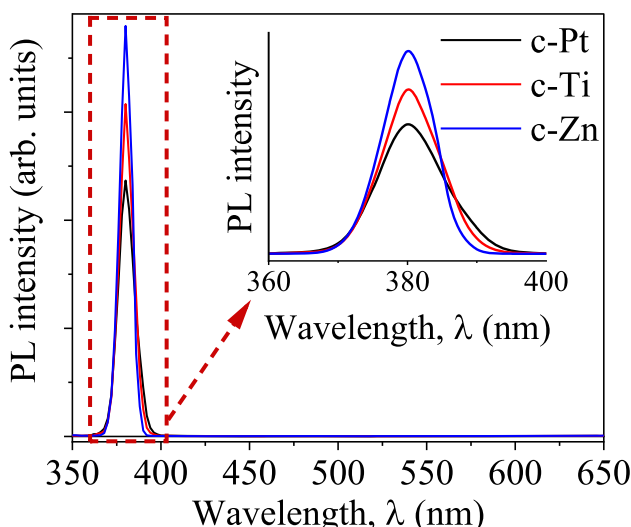


**Fig. 6** Photoluminescence (PL) spectra of TNAs prepared with different CEs. (Inset) The lower value of PL intensity for the 300–500 nm range

second one is the visible emission band [56]. The UV PL peak occurs due to the recombination of photo-generated electrons and holes; on the other hand, the visible emission PL peak (ranging from 400 to 700 nm) associates with deep-level emission such as oxygen vacancies [45]. The PL peaks located at 381 nm (3.16 ~ 3.26 eV) can attribute to the emission of electronic transition near the bandedge [14]. The emission peaks in the UV emission area exhibit the inset of this figure. According to the result, no spike or sharp peak is found in the visible range for c-Pt, c-Zn, and c-Ti. Therefore, all the TNAs samples prepared with the mentioned CEs have no defect states and oxygen vacancies [57].

The surface morphology (SEM image) of TNAs samples prepared with three counter electrodes is shown in Fig. 7. Figure 7a, a1, a2, and a3 shows the top surface, the bottom surface, side view, and length of TNAs prepared with c-Pt materials. TNAs are uniformly grown. The outer diameter and inner diameter of TNAs are  $150 \pm 2$  and  $100 \pm 3$  nm, respectively. Figure 7b exhibits the SEM images of TNAs prepared with Ti counter electrode. Figure 7b1 has the bottom-seed layer. From Fig. 7b2, the TNAs have the outer diameter and inner diameter of  $100 \pm 4$  nm and  $60 \pm 3$  nm, respectively. So that, the wall of the tube is very much robust than others films. On the other hand, Fig. 7c, c1, and c2 shows the surface of cathode Ti, cross-sectional view, and the high-resolution top surface of cathode Ti, respectively, where no significant tubular structures found. The surface is fully porous with thin  $TiO_2$  growing, where cathode ions of anodization potential may be negatively charged. Figure 7d and d1–d6 displays the TNAs, prepared with c-Zn cathode materials. The surface of TNAs is very uniform, as shown in Fig. 7d. From Fig. 7d1 and d3–d6, the double-walled DW-TNAs are grown interestingly, which also indicates the novelty of this work and the unique property of tubes. The TNAs have an outer diameter of  $130 \pm 3$  nm, an inner diameter of  $45 \pm 3$  nm, a thinner outer wall thickness of  $12 \pm 2$  nm, and a thicker inner wall thickness of  $30 \pm 2$  nm.

Figure 7d2 exhibits the bottom surface of DW-TNAs, the existence of DWs recognizes from some broken parts of the TNAs, and the nanotube-in-nanotube structures have been found. The cross section of TNAs is given in Fig. 7d1 & d3, and the length of TNAs has found to be approximately 2  $\mu m$ . Further, the DW-TNAs have characterized by TEM, as shown

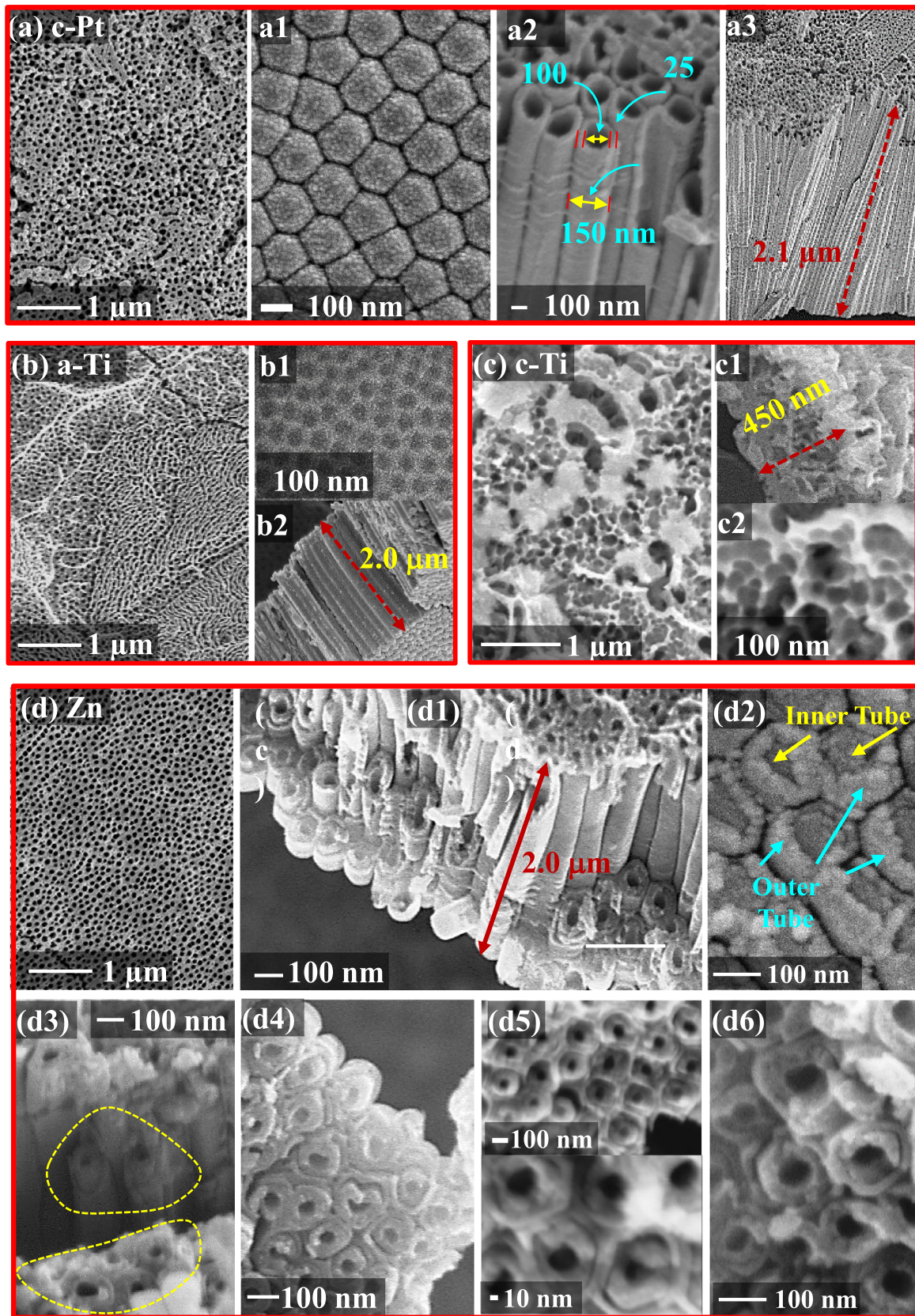


**Fig. 7** The SEM image of TNAs prepared with c-Pt: **a** top surface; (a1) bottom surface; (a2) side view & (a3) cross-sectional view, c-Ti: **b** top surface; (b1) bottom surface; (b2) cross-sectional view; **c** top, (c1) cross-sectional & (c2) high magnified surface of c-Ti, and with c-Zn: **d** top surface; (d1) cross-sectional view; (d2) bottom surface; (d3), (d4), (d5), & (d6) surface of DW-TNAs

in Fig. 8a and b; more evidence of DW structures are found in the individual TNAs. Figure 8c indicates the high-resolution TEM (HRTEM) image. It exhibits a single crystallinity with a neighboring lattice fringe distance of 0.32 nm, which corresponds to the (101) plane in the anatase  $\text{TiO}_2$  phase [55].

It acts that the different CEs lead to fabricating different morphologies due to differences in their overvoltage within the electrolyte [43]. In the above discussion, the  $\text{TiO}_2$  with c-Ti material also has a lower inner and outer diameter of TNA than the TNA with c-Pt material. The general growth mechanism of TNAs prepared with c-Pt and c-Ti materials has been discussed in different kinds of literature [43, 44, 58]. But the possible formation process of DW TNAs with c-Zn can be described as follows. Firstly, a compact  $\text{TiO}_2$  layer forms that barricade further ion transfer after applying a voltage. Then the layer is partially holed by fluoride ion migration and accompanying oxide dissolution [59], and an acceptable porous layer forms. Subsequently, the growth of single-layer TNA and cavities was established under constant voltage anodizing conditions (50 V).

Meanwhile, barrier breakdown happens because of the presence of  $\text{F}^-$  ions under the electric field [58]. When the low-voltage anodization proceeds, small

pits and pores begin and grow in the barrier layer. In addition, fewer  $\text{H}^+$  ions generate, and the pH gradient profile in lower-layer nanotubes becomes less steep. After that, the formation of DW structure TNAs can be achieved [58, 59].

The TNAs are regular, identical, equally spaced, and highly aligned tubes. The porosity ( $P$ ) can control the diffused pollutant molecule inside the catalyst, measured by purely geometrical thoughts [45]. The  $P$  is the counterpart of the surface-solid fraction factor, expressed in the ratio of the surface area of  $\text{TiO}_2$  forming the TNAs and the total surface area of TNAs [23, 54]. When the tubes are close-packed, the porosity equals:

$$P = 1 - \frac{2\pi w(w + D)}{\sqrt{3}(2w + D)^2} \quad (3)$$

where  $w$ ,  $D$ , and  $(2w + D)$  are the wall thickness, pore diameter, and center-to-center distance between TNAs. The roughness factor is calculated from the following equation [54]:

$$\phi_{rf} = \frac{2(1 - P)}{w} = \frac{4\pi(w + D)}{\sqrt{3}(2w + D)^2} \quad (4)$$

Depend on the same geometric model, the rms (root mean square) roughness,  $R_{rms}$  can also be expressed by Eq. (5):

$$R_{rms} = \sqrt{P(1 - P)} \cdot L \quad (5)$$

where  $i$  is the length of TNAs. Table II summarizes the data of the inner and outer diameter of TNAs, the  $R_{rms}$ , and porosity values. The porosity of all TNAs has almost the same value ( $\sim 0.97$ ). But the rms roughness of DW-TNAs prepared with c-Zn is the

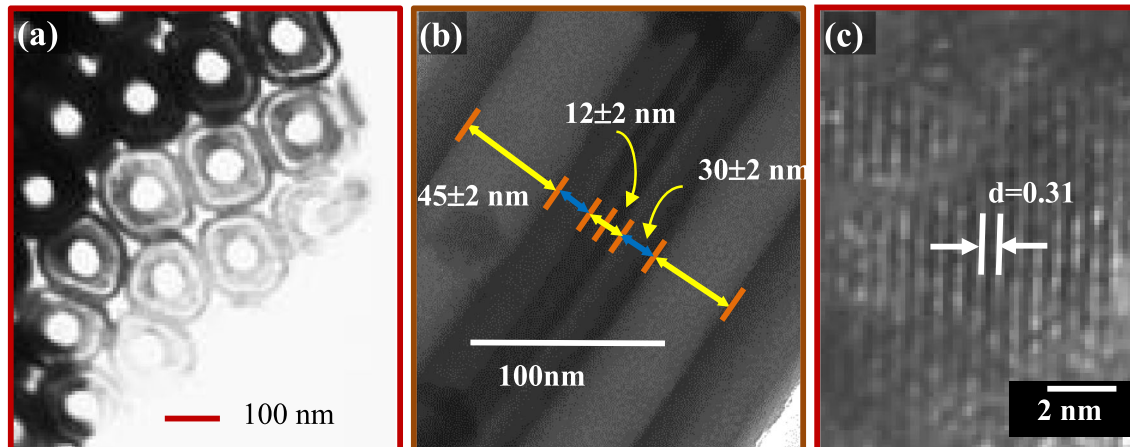
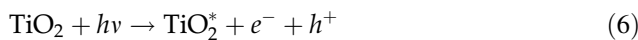


**Fig. 8** The TEM image of TNAs prepared with c-Zn: **a** top surface, **b** cross-sectional view, and **c** HRTEM image of DW-TNAs

highest value of 305.0 nm compared to other cathode materials, which may be due to the DW of TNAs. The  $R_{rms}$  value of TNAs with c-Pt has the lowest value of 295.1 nm. These rms roughness values (312, 335, and 357 nm) have also been justified by the AFM measurement (AFM images have not shown), which are in good agreement with rms data, as shown in Table II. The DW TNAs having a small pore diameter contains a large number of TNAs in an area, compared to other TNAs (with c-Pt & c-Ti), which have large pore diameters containing less number of TNAs in the same area [23]. So, the DW TNAs (with c-Zn) enhance the surface area and improve electron-hole separation for photocatalysis property [24].

Figure 9a shows the degradation mechanism of azoic (MB) dye using TNAs under solar irradiation. When light is incident on the TNAs with the photon energy,  $E_{photon} \geq E_g$ , then TNAs are excited, and the electrons are transferred from valance band (VB) to conduction band (CB) [24] according to the following reaction (6).

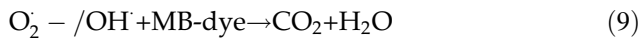


The electrons at the CB lessen the molecular oxygen to superoxide anion free radicals ( $\text{O}_2^-$ ), by Eq. (7).  
 $e^- + \text{O}_2 \rightarrow \text{O}_2^- \quad (7)$

The hole ( $h^+$ ) at the VB reacts with the  $\text{H}_2\text{O}$  molecule, which adsorbs on the surface for generating the hydroxyl free radical ( $\text{OH}^-$ ), according to Eq. (8).



Free radicals  $\text{OH}^-$  and  $\text{O}_2^-$  create a dye solution to decompose the MB-dyes into harmless inorganic like  $\text{H}_2\text{O}$  and  $\text{CO}_2$  due to their strong oxidation power.



Some of the excited electrons at CB are recombined with VB holes on the TNAs, as indicated by Eq. (10), limiting degradation efficiency.



The degradation efficiency (g) of TNAs is calculated from the absorbance of the dye solution at its maximum absorption of the wavelength, as follows:

$$(\%) = \left( 1 - \frac{C}{C_o} \right) \times 100 \quad (11)$$

here,  $C_o$  and  $C$  are the absorbances of the MB-dye solution at light irradiation times of 0 and t, respectively.

The curve of  $C/C_o$  versus illumination time is shown in Fig. 9b, while C shows the concentration of solution extracted out every 20 min. It is a continuous increment in the performance of degradation with the increase of the period of illumination. It observes that the highest peak of absorbance ( $C/C_o$ ) of azoic dye (MB) has occurred at 664 nm, and every category degrades for 2 h (120 min). In the figure,  $C/C_o$  decreases with the increment of time. When Ti cathode materials are used to prepare the TNAs, the photocatalytic activity of MB-dye reduced the value of 0.69 compared to TNAs equipped with Pt counter electrode (0.82), which may be due to the use of the same bandgap of materials (Ti) of both cathode and anode. But, the sample of TNAs fabricated with c-Zn materials has the maximum photodegradation value of 0.97, as shown in Fig. 9c. The improvement of photocatalytic performance may cause a large surface area of DW-TNAs, two bandedge positions (3.15 and 1.78 eV), and more red shift in the optical spectrum [55, 60].

As shown in Fig. 9d, the TNAs fabricated with c-Zn have a high photocatalytic efficiency of 97.0%, which may be caused by the enhancement of the morphology of DW-TNAs red-shifted bandgap toward the visible region. The photocatalytic removal efficiency reached 82.16% and 69.14% after 120 min under illumination for the TNAs fabricated with c-Pt and c-Ti, respectively.

The surface area of TNAs increases with the CEs (c-Pt, c-Ti, and c-Zn) during the anode oxidation method. So, the TNAs lead to prevent the recombination of electron holes. Hence, the lifetime improves the charge carriers [24], increasing the amount of created free radicals and increasing photodegradation efficiency. The kinetics equation of catalytic reaction is to understand the degradation performance of MB-dye using TNAs prepared with different CEs by the first-order model [24, 47],

$$\ln(C_o/C) = -kt \quad (12)$$

where  $k$  indicates the first kinetics equation constant or rate constant. Fitting the curve of degradation performance of MB-dye has been evaluated through the linear regression plotting of the ( $\ln(C/C_o)$ ) versus the irradiation time. The kinetics ( $\ln(C/C_o)$ ) of the

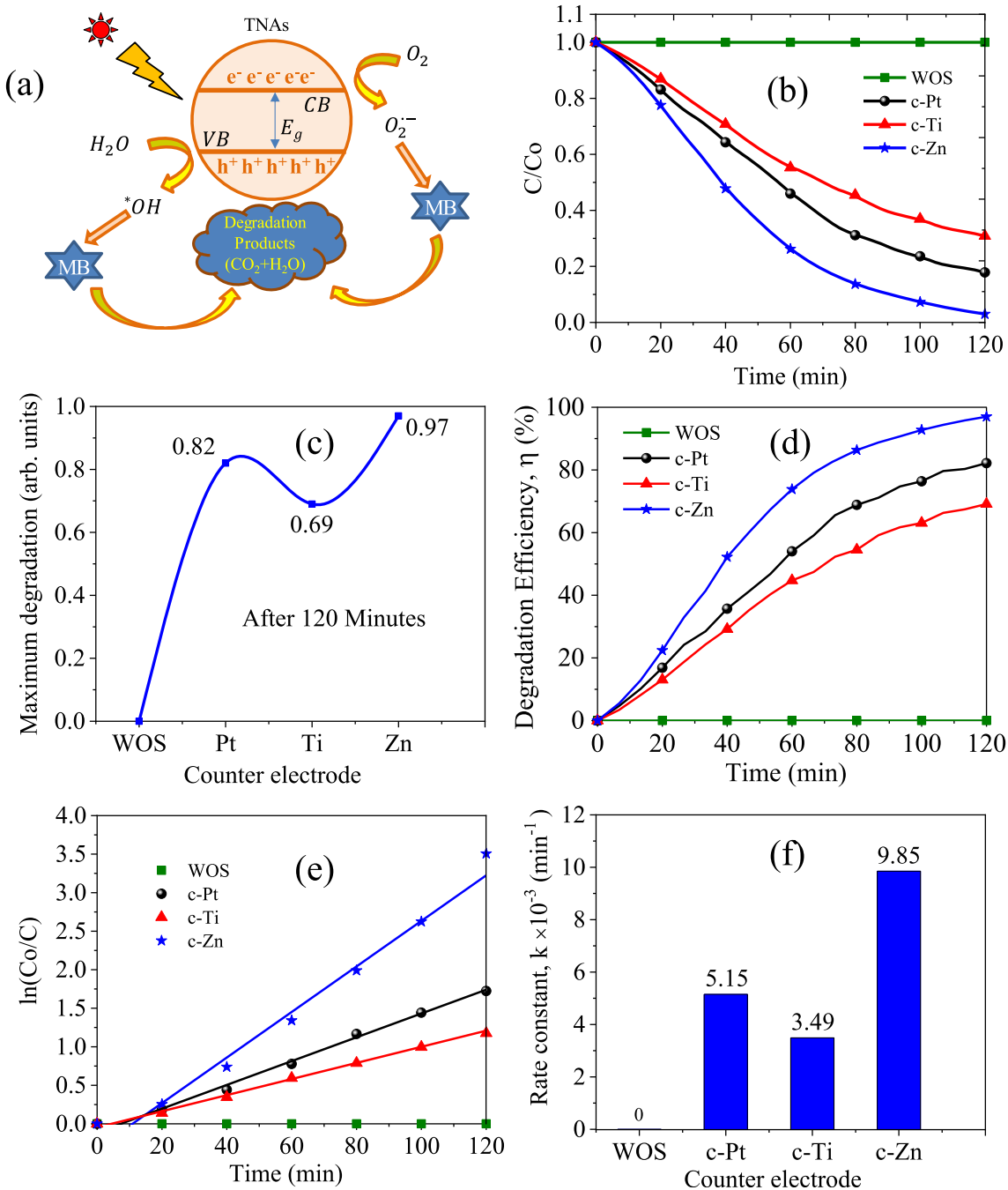


**Fig. 9** **a** The schematic diagram of the photodegradation mechanism. **b**  $C/C_0$  versus time, **c** the maximum degradation value versus CEs, **d** photodegradation efficiency versus time, **e**  $\ln(C_0/C)$  versus time, and **f** rate constant versus CEs curves

photodegradation result is shown in Fig. 7e. The kinetic degradation rate constant ( $k$ ) is calculated from the linear fitting slope, which indicates the uniformity of the photodegradation process. It is observed that the TNAs prepared with c-Ti electrodes have shown the lowest rate, the constant value of  $0.00349 \text{ min}^{-1}$ , than the TNAs, prepared with

other CEs of (c-Pt & c-Zn). The TNAs with c-Ti cause the degradation rate to be very slow, which may be due to less surface area with its low absorption edge. The TNAs with c-Pt have the rate constant value of  $0.00515 \text{ min}^{-1}$ , which means that the photodegradation value is better than the other researcher's data [15, 23, 61, 62]. It is observed that the value of  $k$  for

**Table 3** The TNAs thickness, degradation efficiency, rate constant k, and regression coefficients (R) of MB degradation using TNAs prepared with different counter electrodes

CEs	Thickness (μm)	Maximum degradation efficiency (%)	Rate constant (min <sup>-1</sup> )	Regression coefficient R	Coefficient of determination (R <sup>2</sup> )
c-Pt	2.10	82.2	0.00515	0.9959	0.9918
c-Ti	2.05	69.1	0.00349	0.9983	0.9966
c- Zn	2.10	97.0	0.00985	0.9922	0.9844

**Table 4** Comparative photodegradation data of proposed TNAs with other researcher's data

	Fabrication parameters	Maximum degradation	Rate constant (min <sup>-1</sup> )	Reference
TNAs	50 V + NH <sub>4</sub> F (0.3 wt%) + H <sub>2</sub> O (2 vol%) + Pt	0.49	0.005	[23]
TNAs	40 V + NH <sub>4</sub> F (0.3 wt%) + Pt	0.47	0.0045	[41]
TNAs	20 V + [NH <sub>4</sub> F + (NH <sub>4</sub> ) <sub>2</sub> SO <sub>4</sub> ] (0.27 wt%) + H <sub>2</sub> O (3 vol%) + Pt	0.44	0.0046	[42]
TNAs	80 V + NH <sub>4</sub> F (0.5 wt%) + H <sub>2</sub> O (3 vol%) + Pt	0.48	0.0043	[55]
TNAs	50 V + NH <sub>4</sub> F (0.3 wt%) + H <sub>2</sub> O (3 vol%) + c-Pt	0.82	0.00515	This work
DW- TNAs	50 V + NH <sub>4</sub> F (0.3 wt%) + H <sub>2</sub> O (3 vol%) + c-Zn	0.97	0.00985	This work

DW-TNAs prepared with c-Zn has the highest rate constant value of 0.00985 min<sup>-1</sup> under sunlight illumination. The high DW-TNAs possess the fastest degradation rate of MB because many carriers are available for effective photo-oxidation.

Table 3 summarizes the data of TNAs thickness, degradation efficiency, rate constant (k), and the regression coefficients (R) of MB-dye degradation using TNAs prepared with different counter electrodes. The regression coefficient, R, and R<sup>2</sup> of TNAs prepared with c-Ti material have a significant value of 0.9983 and 0.9966, respectively, indicating low photodegradation efficiency. Whereas the sample of TNAs with c-Zn obtained the lowest value of R and R<sup>2</sup> as 0.9922 and 0.9844, respectively. The high TNAs with c-Zn electrodes keep the fast degradation rate of MB-dye due to many carriers that are available for the effective photo-oxidation process [24]. Table 4 exhibits a comparison between the proposed work and other researcher's works, which is the new finding of good degradation efficiency using TNAs with a c-Zn electrode in sunlight due to two

absorption edge as well as red-shifted bandgap value [5].

#### 4 Conclusion

The highly aligned TNAs were successfully fabricated by anode oxidation method with NH<sub>4</sub>F-based electrolyte and different CEs (c-Pt, c-Ti, and c-Zn). The TNAs synthesized c-Zn materials red-shifted absorption edge with two bandgaps of 3.15 eV and 1.78 eV. The CEs variations greatly influenced the size and shape of TNAs during the anode oxidation method. The main uniqueness and novelty of this work were to prepare DW-TNAs with c-Zn CEs during the anode oxidation method. The DW-TNAs had an outer diameter of 130 ± 3 nm, thinner outer wall thickness of 12 ± 2 nm, and thicker inner wall thickness of 30 ± 2 nm. The TNAs sample fabricated with c-Ti have a low photodegradation performance. The TNAs prepared with c-Zn exhibited the highest rms roughness value of 305.0 nm (357 nm by AFM),

photodegradation efficiency of 97.0%, and rate constant value of  $0.00985 \text{ min}^{-1}$  than the TNAs c-Pt, c-Ti materials, and other researcher's data. This work had proved that the DW-TNAs (prepared with c-Zn) were a re-usable photocatalyst for efficient degradation of azoic (MB) dye from wastewater.

## Acknowledgements

This Project was funded by the Deanship of Scientific Research (DSR) at King Abdulaziz University, Jeddah, under Grant No. G: 526-135-1439. The authors, therefore, acknowledge with thanks DSR for technical and financial support.

## References

- J.A. Torres-Luna, G.I. Giraldo-Gómez, N.R. Sanabria-González, J.G. Carriazo, Bull. Mater. Sci. (2019). <https://doi.org/10.1007/s12034-019-1817-1>
- S. Vignesh, S. Suganthi, J. Kalyana Sundar, V. Raj, Appl. Surf. Sci. **488**, 763 (2019)
- S.M. Hosseinpour-Mashkani, A. Sobhani-Nasab, J. Mater. Sci. Mater. Electron. **28**, 4345 (2017)
- V. Shanmugam, K.S. Jeyaperumal, P. Mariappan, A.L. Muppudathi, New J. Chem. **44**, 13182–13194 (2020)
- A. Singh, P. Khare, S. Verma, A. Bhati, A.K. Sonker, K.M. Tripathi, S.K. Sonkar, A.C.S. Sustain, Chem. Eng. **5**, 8860 (2017)
- J.A. Torres-Luna, J.G. Carriazo, N.R. Sanabria, Environ. Technol. **37**, 1346–1356 (2016)
- N. Caner, I. Kiran, S. İlhan, A. Pinarbasi, C.F. Iscen, Sep. Sci. Technol. **46**, 2283–2290 (2011)
- K. Balapure, N. Bhatt, D. Madamwar, Bioresour. Technol. **175**, 1–7 (2015)
- W.M. Abd El-Rahim, H. Moawad, A.Z. Abdel Azeiz, M.J. Sadowsky, J. Biotechnol. **260**, 11–17 (2017)
- F. Bouatay, S. Dridi-Dhaouadi, N. Drira, M. Farouk Mhenni, Desalin. Water Treat. **57**, 13561–13572 (2016)
- S.P. Ghuge, A.K. Saroha, J. Water Process Eng. **23**, 217 (2018)
- J. Fu, G.Z. Kyzas, Cuihua Xuebao/Chin. J. Catal. **35**, 1 (2014)
- N.N. Patil, S.R. Shukla, J. Water Process Eng. **7**, 314–327 (2015)
- C. Fonseca Couto, L.C. Lange, M.C. Santos Amaral, J. Water Process Eng. **26**, 156–175 (2018)
- B. Bayarri, J. Giménez, D. Curcó, S. Esplugas, Catal. Today **101**, 227–236 (2005)
- A.Y. Shan, T.I.M. Ghazi, S.A. Rashid, Appl. Catal. A **389**, 1–8 (2010)
- B. Paul, W.N. Martens, R.L. Frost, Appl. Clay Sci. **57**, 49–54 (2012)
- M.R. Elahifard, M.R. Gholami, Environ. Prog. Sustain. Energy **31**, 371–378 (2012)
- L. Kuang, Y. Zhao, W. Zhang, S. Ge, J. Environ. Eng. (2016). [https://doi.org/10.1061/\(ASCE\)EE.1943-7870.0001032](https://doi.org/10.1061/(ASCE)EE.1943-7870.0001032)
- M. Ramezani, S.M. Hosseinpour-Mashkani, J. Electron. Mater. **46**, 1371 (2017)
- Z. Aghajani, S.M. Hosseinpour-Mashkani, J. Mater. Sci. Mater. Electron. **31**, 6593 (2020)
- S. Vignesh, A.L. Muppudathi, J.K. Sundar, J. Mater. Sci. Mater. Electron. **29**, 10784 (2018)
- I.M. Mehedi, M.F. Hossain, T. Takahashi, M.S. Islam, J. Photochem. Photobiol. A **335**, 200–210 (2017)
- M. Shaban, A.M. Ahmed, N. Shehata, M.A. Betiba, A.M. Rabie, J. Colloid Interface Sci. **555**, 31 (2019)
- M.L. Tran, C.-C. Fu, R.-S. Juang, J. Mol. Liq. **276**, 32–38 (2019)
- M. Khodadadi, M.H. Ehrampoush, M.T. Ghaneian, A. Allahresani, A.H. Mahvi, J. Mol. Liq. **255**, 224–232 (2018)
- M.R.S. Joice, T.M. David, P. Wilson, J. Phys. Chem. C **123**, 27448–27464 (2019)
- L. Laysandra, M.W.M.K. Sari, F.E. Soetaredjo, K. Foe, J.N. Putro, A. Kurniawan, Y.-H. Ju, S. Ismadji, Heliyon **3**, e00488 (2017)
- B. Sathyaseelan, E. Manikandan, V. Lakshmanan, I. Basakaran, K. Sivakumar, R. Ladchumananandasivam, J. Kennedy, M. Maaza, J. Alloys Compd. **671**, 486–492 (2016)
- F. Fang, J. Kennedy, E. Manikandan, J. Futter, A. Markwitz, Chem. Phys. Lett. **521**, 86 (2012)
- C.W. Lai, J.C. Juan, W.B. Ko, S. Bee Abd Hamid, Int. J. Photoenergy (2014). <https://doi.org/10.1155/2014/524135>
- Y. Ji, K.-C. Lin, H. Zheng, J. Zhu, A.C.S. Samia, Electrochim. Commun. **13**, 1013–1015 (2011)
- S. Yang, Y. Liu, C. Sun, Appl. Catal. A **301**, 284–291 (2006)
- S.-I. Na, S.-S. Kim, W.-K. Hong, J.-W. Park, J. Jo, Y.-C. Nah, T. Lee, D.-Y. Kim, Electrochim. Acta **53**, 2560–2566 (2008)
- X. Wu, Q.-Z. Jiang, Z.-F. Ma, M. Fu, W.-F. Shangguan, Solid State Commun. **136**, 513–517 (2005)
- E. Coy, K. Siuzdak, M. Pavlenko, K. Załęski, O. Graniel, M. Ziółek, S. Balme, P. Miele, M. Weber, M. Bechelany, I. Iatsunskyi, Chem. Eng. J. **392**, 123702 (2020)
- G.K. Mor, O.K. Varghese, M. Paulose, C.A. Grimes, Adv. Funct. Mater. **15**, 1291–1296 (2005)
- M.F. Hossain, S. Biswas, Z.H. Zhang, T. Takahashi, J. Photochem. Photobiol. A **217**, 68–75 (2011)
- H.-F. Zhuang, C.-J. Lin, Y.-K. Lai, L. Sun, J. Li, Environ. Sci. Technol. **41**, 4735–4740 (2007)

40. S. Berger, R. Hahn, P. Roy, P. Schmuki, *Phys. Status Solidi* **247**, 2424–2435 (2010)
41. C.-J. Lin, Y.-H. Yu, S.-Y. Chen, Y.-H. Liou, *World Acad. Sci. Eng. Technol.* **65**, 1094 (2010)
42. X. Zhao, Y. Zhu, Y. Wang, L. Zhu, L. Yang, Z. Sha, *J. Nanomater.* (2015). <https://doi.org/10.1155/2015/104193>
43. N.K. Allam, C.A. Grimes, *Sol. Energy Mater. Sol. Cells* **92**, 1468–1475 (2008)
44. S. Sreekantan, K.A. Saharudin, L.C. Wei, *I.O.P. Conf. Ser. Mater. Sci. Eng.* (2011). <https://doi.org/10.1088/1757-899X/21/1/012002>
45. K. Indira, U.K. Mudali, T. Nishimura, N. Rajendran, *J. Bio-Triblo-Corros.* (2015). <https://doi.org/10.1007/s40735-015-0024-x>
46. W.-C. Chen, M.-H. Yeh, L.-Y. Lin, R. Vittal, K.-C. Ho, *A.C.S. Sustain. Chem. Eng.* **6**, 3907–3915 (2018)
47. Z. Zhang, M.F. Hossain, T. Takahashi, *Appl. Catal. B* **95**, 423–429 (2010)
48. S. Ozkan, N.T. Nguyen, A. Mazare, I. Cerri, P. Schmuki, *Electrochem. Commun.* **69**, 76–79 (2016)
49. K.R. Hebert, S.P. Albu, I. Paramasivam, P. Schmuki, *Nat. Mater.* **11**, 162–166 (2012)
50. B.D. Cullity, *Elements of X-Ray Diffraction* (Addison-Wesley, Boston, 1978)
51. S. Kahraman, H.M. Çakmak, S. Çetinkaya, F. Bayansal, H.A. Çetinkara, H.S. Güder, *J. Cryst. Growth* **363**, 86–92 (2013)
52. M.F. Hossain, T. Takahashi, *J. Nanosci. Nanotechnol.* **11**, 3222–3228 (2011)
53. M.F. Hossain, S. Naka, H. Okada, *J. Photochem. Photobiol. A* **360**, 109–116 (2018)
54. K. Zhu, N.R. Neale, A. Miedaner, A.J. Frank, *Nano Lett.* **7**, 69–74 (2007)
55. H. Wu, Z. Zhang, *Int. J. Hydrog. Energy* **36**, 12923–12931 (2011)
56. A.E. Riad, F.D. Barlow, ISHN, *Thin Film Technology Handbook*, 1st edn. (McGraw-Hill Professional, New York, 1998)
57. M.F. Hossain, T. Takahashi, *IEEE Trans. Nanotechnol.* **13**, 755–759 (2014)
58. Y. Ji, *RSC Adv.* **4**, 62698–62707 (2014)
59. D. Guan, P.J. Hymel, Y. Wang, *Electrochim. Acta* **83**, 420–429 (2012)
60. Z. Zhang, M.F. Hossain, T. Takahashi, *Mater. Lett.* **64**, 435–438 (2010)
61. Y. Zhang, Y. Guo, G. Zhang, Y. Gao, *Appl. Clay Sci.* **51**, 335–340 (2011)
62. M.N. Chong, B. Jin, C.W.K. Chow, C. Saint, *Water Res.* **44**, 2997–3027 (2010)

**Publisher's Note** Springer Nature remains neutral with regard to jurisdictional claims in published maps and institutional affiliations.